



High performance hierarchical SiCN nanowires for efficient photocatalytic - photoelectrocatalytic and supercapacitor applications

I. Neelakanta Reddy^{a,*1}, Adem Sreedhar^b, Ch. Venkata Reddy^a, Jaesool Shim^{a,*}, Migyung Cho^{c,1}, Kisoo Yoo^{a,**}, Dongseob Kim^{d,**}, Jin Seog Gwag^b

^a School of Mechanical Engineering, Yeungnam University, Gyeongsan, 712-749, South Korea

^b Department of Physics, Yeungnam University, Gyeongsan, 712-749, South Korea

^c School of Information Engineering, Tongmyong University, Busan, 608-711, South Korea

^d Aircraft System Technology Group, Korea Institute of Industrial Technology, Gyeongbuk-do, 38822, South Korea



ARTICLE INFO

Keywords:

High energy ball milling
Nanowire morphology
Charge carrier dynamics
Supercapacitor
Photocatalytic-photoelectrocatalytic

ABSTRACT

We synthesized SiCN nanowires by a combination of high-energy ball milling and post-heat treatment using high-purity silicon and carbon nanopowders (< 100 nm), and evaluated the effects of process parameters on their structural, chemical, optical properties, photoelectrocatalytic and photocatalytic activities. Cubic SiCN crystal phase with a lattice constant of 4.35 Å was observed. The optical bandgap of 2.20 eV was observed with nanowire diameters ranging from 23 nm to 37 nm. The SiCN nanowires showed good photocatalytic activity with the highest degradation percentage of ~99% in 40 min for the degradation of Rhodamine B dye under visible light, and a degradation rate of 0.0841 min⁻¹. The SiCN nanowires showed no significant reduction in photocatalytic activity for five consecutive cycles, indicating that they are extremely stable against organic dyes. The SiCN nanowires were used for photoelectrochemical water splitting and the effect of electrolytes was studied. The highest photocurrent density of 5 × 10⁻² mAcm⁻² vs. Ag/AgCl in 0.1 M KOH solution was achieved owing to the improved visible light collection and electron hole separation. The exchange current density, Tafel slopes, and limiting diffusion current density were found to be 3.17 mAcm⁻², 68.13 mVdec⁻¹, and 1.54 mAcm⁻², respectively. Further, the specific capacitance of the SiCN nanowires was estimated, obtained of 188 mFcm⁻² at a current density of 5 mAcm⁻².

1. Introduction

Photoelectrochemical (PEC) hydrogen production from pure water is viewed as one of the holy grails of hygienic and renewable energy resources from both ecological and commercial points of view [1]. Intensive research efforts have been triggered following the demonstration of water splitting with TiO₂ as a catalyst material, under UV illumination in 1971 [2]. However, until today, the understanding of highly efficient commercial photoelectrocatalytic hydrogen generation from pure water remains a considerable challenge, and less consistent improvements have been made in this arena [3–6]. Moreover, materials with dual applications are highly desired for current global applications in order to reduce the time and cost of commercialization.

In recent years, a great deal of attention has been focused on the development of silicon-based nanostructures because of their potential applications in the semiconductor industry. Nanostructures, with

bandgaps changeable over a wide energy range, are of specific interest in photocatalyst technology. For instance, Si quantum dots, SiC, Si₃N₄, and SiO₂ have been examined as photocatalytic materials to produce hydrogen from water or to degrade organic pollutants [7–10]. Researchers have reported that Si-based catalyst materials show improved activity compared with traditional photocatalysts (TiO₂, ZnO, CdS, GaP, and WO₃) [8,11]. In the family of Si-based nanostructures, both SiC and Si₃N₄ are outstanding materials possessing several attractive properties such as a wide optical bandgap, good chemical stability, high electron mobility, and good thermal stability. Indeed, the optical bandgap of SiC is in the range 2.90–3.20 eV while that of Si₃N₄ is near ~5.0 eV, suggesting that ternary SiCN can be a photoelectron material with a variable bandgap between 2.90 and 5.0 eV. Therefore, ternary SiCN nanostructures have been proven to have great potential for applications in the semiconductor industry and can serve as a stable structural material. SiCN is prepared using various techniques such as microwave

* Corresponding authors.

** Corresponding authors.

E-mail addresses: neela.sra@gmail.com (I.N. Reddy), jshim@ynu.ac.kr (J. Shim), kisoo.yoo@yu.ac.kr (K. Yoo), yusae@kitech.re.kr (D. Kim).

¹ These authors contributed equally.

plasma-enhanced chemical vapor deposition (CVD) [12], radio frequency CVD [13], and reactive magnetron sputtering [14]. Tomasella et al. [15], and Peng et al. [16] studied the structural and optical properties of SiCN. To the best of our knowledge, there are no published data on the photocatalytic and photoelectrocatalytic activities of SiCN nanowire nanostructures under visible light illumination. Thus, for the first time, we report on the preparation of SiCN nanowires via pulverizing and post-heat treatment in order to understand the effects of these nanostructures on the degradation of organic dyes and water splitting for hydrogen generation.

SiCN nanostructures have a remarkable advantage as an energy storage material owing to their high thermodynamic and chemical stability. In addition, these consist of graphene-like carbon chains wrapped domains of silicon nitride or silicon carbide [17]. Crystalline Si-based anodes generally do not suffer from large variations in volume owing to their lower density. A few researchers have investigated the energy performance of SiCN material [18,19]. Kolb et al. performed electrochemical analysis of amorphous SiCN prepared from commercially available graphite powder [18]. SiCN structures derived from polysilylenediamine using pyrolysis as an anode in lithium batteries was studied by Su et al. [19]. A clear gap exists in the understanding of the performance of crystalline SiCN nanostructures for capacitor applications. Thus, we investigated the supercapacitor properties of crystalline SiCN nanowire nanostructures.

In this paper, we synthesized SiCN nanowires via a combination of high-energy ball milling and post-annealing techniques, and investigated their structure, morphology, and electronic structure, amongst others. Dye degradation was studied by degrading Rhodamine B (RhB) dye under visible light illumination to observe photocatalytic activity. Photoelectrocatalytic characteristics were investigated by recording Tafel plots, cyclic voltammograms (C-V), time-resolved photocurrent ($I-t$), and linear sweep voltammograms (I-V) with a conventional three-electrode cell. Further, the photocurrent responses of SiCN nanowires in various electrolytes such as Na_2SO_4 , NaOH , and KOH were also investigated. Supercapacitance properties such as cyclic voltammetry (CV) and galvanostatic charging/discharging (GCD) were investigated in a 0.1 M KOH electrolyte using a conventional three-electrode electrochemical workstation, and the specific capacitance of SiCN nanowires from both CV and GCD were estimated.

2. Experimental

2.1. Synthesis of SiCN nanowires

To synthesize SiCN nanowires, silicon powder (> 99.90%) and carbon powder (99.95%) supplied by Sigma-Aldrich were used as raw materials. The mixed powder was loaded into a 100 mL molybdenum vial at mole ratio of 1:1, and 6 mm-diameter molybdenum balls were introduced into the vial. The weight ratio of the ball to powder was set at 20:1. High-energy milling was carried out by a planetary ball mill at a speed of 1200 rpm for 60 h. The milled powder was poured into an alumina crucible and then heat treated in the presence of nitrogen at 1000, 1200, 1400, and 1600 °C for 4 h. A schematic of the synthesis of SiCN nanowires is shown in Fig. 1.

2.2. Characterization

A Rigaku X-ray diffractometer with $\text{Cu K}\alpha$ radiation operated at 30 kV and 100 mA, with a scanning speed of 3° min^{-1} and step width of 0.02° (with a $\text{Cu K}\beta$ filter) was used for the phase analysis of the prepared samples. The morphology was investigated in detail by scanning electron microscopy (SEM, Carl Zeiss; Germany) and high-resolution transmission electron microscopy (TEM; G2 F30 S-Twin). The optical properties at room temperature were recorded with a UV-vis spectrometer (Cary 5000, USA), Horiba photoluminescence spectrometer (iHR-550; 325 nm), and Raman spectrometer (XploRA Plus; 532 nm).

Fourier-transform infrared (FT-IR; Perkin Elmer spectrum100) spectroscopy was used for FT-IR analysis. X-ray photoelectron spectroscopy (XPS; Thermo Fisher Scientific MultiLab 2000) was utilized to study the oxidation states of the samples.

2.3. Dye degradation studies

The photocatalytic activities of the SiCN nanowires were studied via the photo-degradation of a diluted solution of RhB under visible light. A 10 ppm RhB solution containing 60 mg of catalyst was mixed with a stirrer in the dark at room temperature for 60 min to obtain an equilibrium mixture. Then, it was transferred to a double-walled jar and exposed to visible light. During treatment, constant stirring was maintained to keep the mixture in suspension. The temperature of the double-walled jar was kept constant at 30 °C by circulating water using a water chiller. The changes in the RhB concentration was determined by monitoring the intensity of the RhB peak at 554 nm using the UV-Vis spectrometer. Observations were made every 10 min by collecting the RhB solution from the photocatalytic reactor and centrifuging it to eliminate the catalyst. The tests were repeated to ensure the reliability of the results and confirm the reusability of the material.

2.4. Photoelectrochemical and capacitance measurements

2.4.1. Photoelectrochemical studies

The electrochemical analysis was carried out with a three-electrode instrument in different electrolytes such as Na_2SO_4 , KOH , and NaOH at 0.1 M concentration, via electrochemical impedance spectroscopy (SP-200 Potentiostat; Bio-Logic). Ag/AgCl and platinum electrodes were used as the reference electrode and counter electrodes, respectively. The prepared electrode with SiCN nanowires was used as the working electrode. This working electrode was prepared by mixing 9 mg of SiCN nanowires with 120 μL of ethanol glycol followed by continuous sonication for 3 h to obtain a uniform solution. The stirred solution was used to prepare thin films on indium tin oxide (ITO)-coated glass ($2 \times 2 \text{ cm}^2$) by spin coating at 2000 rpm. To obtain each monolayer, 20 μL of solution was used and the film was dried at 200 °C for 60 min on a hot plate. Similarly, the process was repeated twice per sample and dried as mentioned above. The samples obtained were masked, leaving an active area of 1 cm^2 and used as a working electrode. The PEC activity of SiCN nanowires was examined by cyclic voltammetry (C-V), linear sweep voltammetry (I-V) and time-resolved photocurrent ($I-t$) measurements.

2.4.2. Capacitance studies

CV and GCD of SiCN nanowires were analyzed at room temperature using a conventional three-electrode quartz cell (SP-200 Potentiostat; Bio-Logic; France) consisting of the as-prepared SiCN sample as the working electrode (anode) for investigation, and Ag/AgCl and Pt as the reference and counter (cathode) electrodes, respectively, in a 0.1 M KOH aqueous solution as the electrolyte. The anode was prepared as mentioned in the photoelectrochemical studies. In CV and GCD, the applied potential window was varied from -0.10 V to 0.50 V . The specific capacitance was estimated from the discharging curves and CVs according to the formulas:

$$C_s = \frac{1}{A\vartheta\Delta V} \int i(V)dV \quad (1)$$

$$C_s = \frac{I\Delta t}{A\Delta V} \quad (2)$$

where C_s is the specific capacitance of SiCN nanowires, A is the active area of SiCN nanowires coated on the ITO substrate, ϑ is the scan rate, ΔV is the applied potential window in the CV curves and discharging process, $i(V)$ is the current, I is the applied current, and Δt is the discharging time [20].

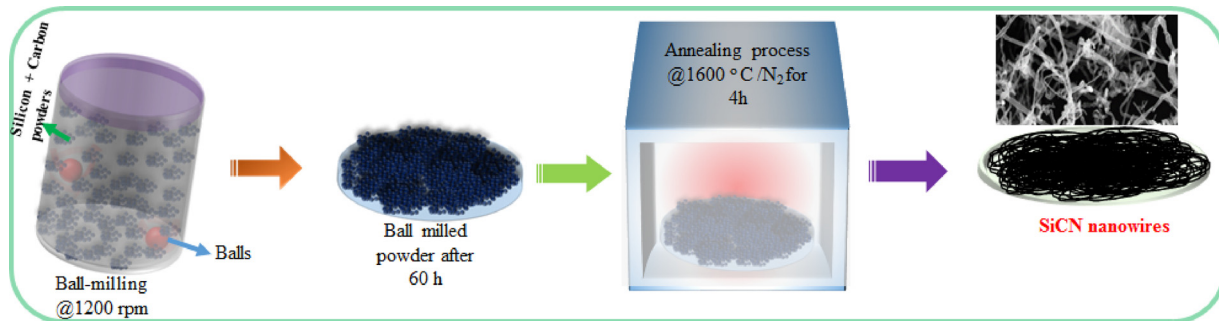


Fig. 1. Schematic representation of the SiCN nanowire synthesis.

3. Results and discussion

3.1. Phase analysis

The phase analysis of SiCN nanowires synthesized via the ball milling and heat treatment is shown in Fig. S1 observed lone Si peaks. To achieve pure SiCN crystalline phase, the ball-milled powder samples were subjected to post-annealing temperatures 1000, 1200, 1400 and 1600 °C, respectively. As shown in Fig. 2, at below 1200 °C, only Si peaks positioned at 28.48°, 47.34°, 56.16°, 69.14°, and 76.34° are observed, which indicates that no SiCN phase is formed. As the heat treatment temperature increases to 1400 °C, the SiCN peaks begin to appear along with the Si peaks; however, the intensities of the SiCN peaks are lower than those of the Si peaks. The sample heat-treated at 1600 °C shows the existence of only SiCN crystalline phase with peak positions at 35.72°, 41.54°, 60.14°, and 71.86° corresponding to the (111), (220), (220), and (311) planes, respectively. The peaks are related to the cubic phase of SiCN as per JCPDS file No.: 74-2308 with the

space group of F23. The calculated lattice constant is 4.35 Å, which is close to the standard lattice constant of SiCN (4.36 Å). Sigh et al. [21] observed similar peak positions for the same planes of SiCN thin films grown by radio-frequency magnetron sputtering for non-volatile memory device applications. The highly intense diffraction peaks reveal that the SiCN formed is highly crystalline in nature. Further, no foreign phases appeared in the sample post-heat-treated at 1600 °C, indicating the good quality of the samples. The clear formation or transformation of the SiCN phase with post-heat treatment is clearly observed in the results of XRD analysis. Further, the crystallite size was estimated to be ~87 nm using Scherer's formula [22], considering the high-intensity peak positioned at 35.72° (111). The results obtained from the structural analysis showed good agreement with those reported in literature [23–25].

3.2. Morphology analysis

The morphologies of post-annealed samples were investigated by

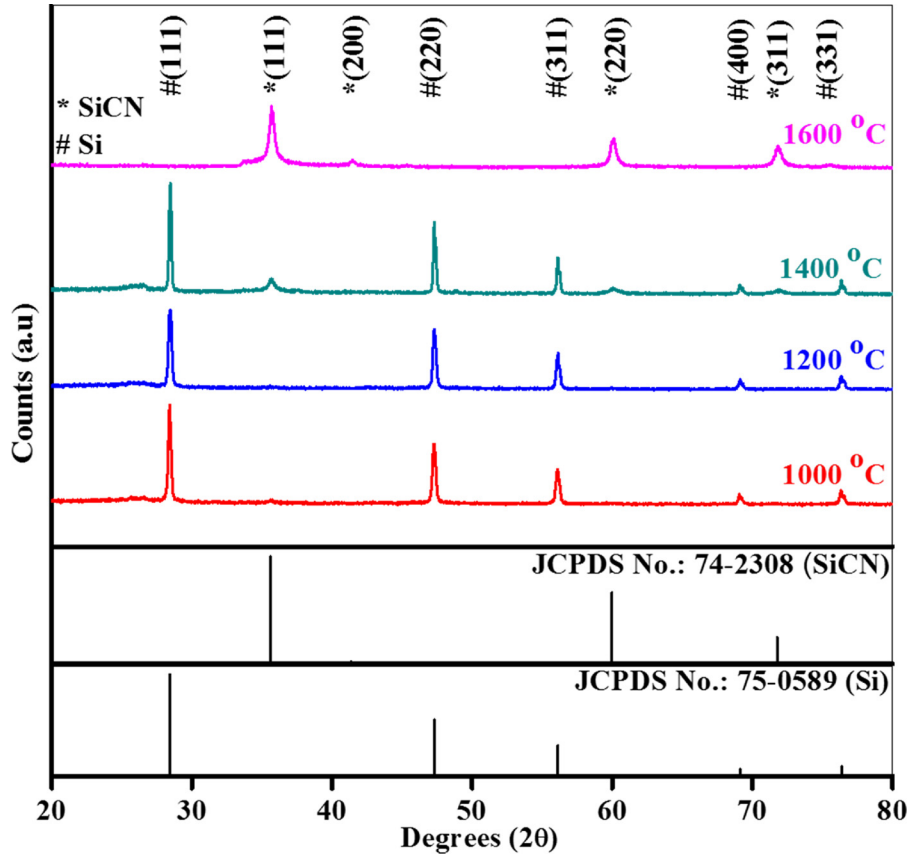


Fig. 2. XRD analysis of SiCN nanowires.

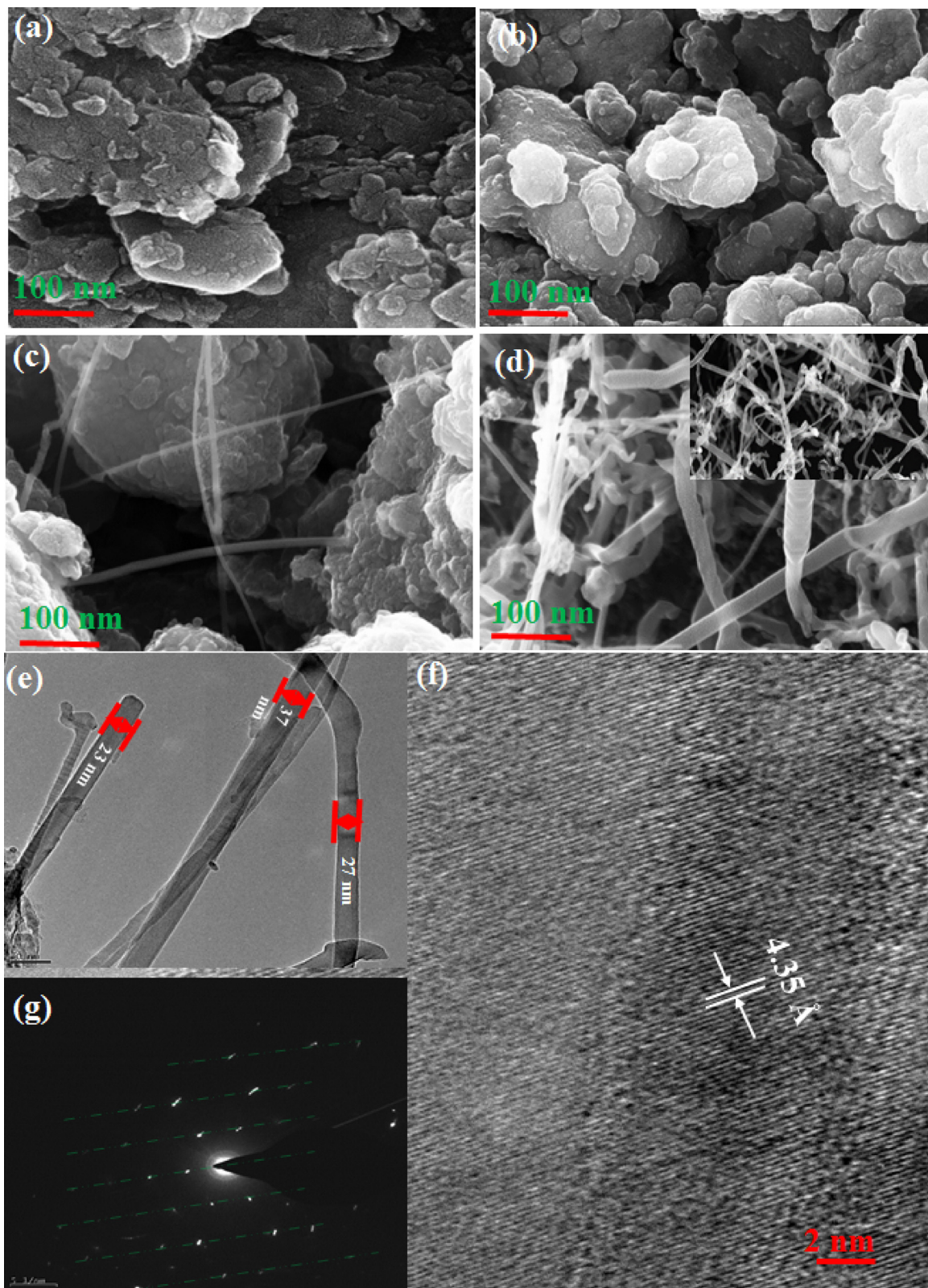


Fig. 3. The morphology of SiCN nanowires: (a–d) SEM analysis, and (e–g) HR-TEM analysis.

SEM and HR-TEM (Fig. 3). The SEM images of samples post-annealed at 1000 and 1200 °C are shown in Fig. 3(a–b), where no nanostructure formation is observed, suggesting that the annealing temperature is not adequate to produce SiCN nanostructures. Fig. 3(c) reveals the morphology of a sample post-annealed at 1400 °C, where the initiation of

SiCN nanowire formation is observed, and the results are consistent with those of the structural analysis. However, a major portion of the sample showed morphology similar to that of samples post-annealed at lower temperatures. To achieve fully formed SiCN nanowires, the samples were subjected to further annealing at 1600 °C, (Fig. 3(d)).

Well-grown SiCN nanowires with various diameters are observed in the SEM image. Cai et al. [26] observed ultra-long SiCN nanowires synthesized by the pyrolysis of hexamethyldisilazane at 1200 °C. The morphology of SiCN observed in the present study is consistent with those published previously [23,27].

The HR-TEM images of the samples post-annealed at various temperatures are shown in Fig. S2 and Fig. 3(e–g). From Fig. S2, no nanostructures were observed in the samples post-annealed at 1000 and 1200 °C. In the case of the sample post-annealed at 1400 °C, shows an initiation of nanowires and the results correlated well with the XRD and SEM analysis. The low-magnification HR-TEM images of the sample post-annealed at 1600 °C shown in Fig. 3(e), indicate that the sample has a fully grown nanowire structure with different sizes ranging from 23 nm to 37 nm. The HR-TEM image in Fig. 3(f) shows well-distinguished lattice fringes of the SiCN nanowires, confirming the presence of a crystalline phase; the results agree with those of structural analysis. The distance between the lattice fringes is identified to be 4.35 Å, which matches the standard lattice constant of SiCN (4.36 Å) as per JCPDS file No.: 74-2308. This estimated lattice constant is also consistent with the results of XRD analysis. The selected area diffraction (SAED) pattern provides evidence of the crystallinity and crystal direction. The SAED pattern of the sample post-annealed at 1600 °C is shown in Fig. 3(g). The characteristic line patterns of a nanowire are observed, and this result is consistent with the results of SEM analysis.

3.3. Optical analysis

The absorptance spectrum was recorded to identify the optical

bandgap of the samples post-annealed at 1600 °C. The optical bandgap of the SiCN nanowires is estimated as ~2.20 eV (Fig. 4(a)). The infrared spectrum of the SiCN nanowires is shown in Fig. 4(b). According to the reported results [23,28–31], the IR spectrum of the sample have distinct and characteristic absorption peaks of the $\text{Csp}^3\text{-H}$ bond located at 2980 and 2897 cm^{-1} , C-N band at 2100 cm^{-1} , C=C or C=N band at 1506 and 1487 cm^{-1} , and Si-C band at 780 and 618 cm^{-1} ; these absorption bands originated from the SiCN nanowires. In this study, we observed fewer organic groups than that reported previously [32,33], indicating the quality of the prepared SiCN nanowires. The Raman analysis of the sample post-annealed at 1600 °C is presented in Fig. 4(c). The Raman peaks of SiCN can be attributed to three main vibrational bands: viz., 150–700, 700–1275, and 1275–1730 cm^{-1} [34]. The bands between 150 and 700 cm^{-1} are attributed to the Si grid adapted with the assistance of carbon and nitrogen atom; the 700–1275 cm^{-1} band region corresponds to Si-N , C-N , and carbon from the T band; and the 1275–1730 cm^{-1} band region can be assigned to carbon and its bonding add-on with Si and N. We observed the Raman vibrational bands in the range 700–1275 and 1275–1730 cm^{-1} located specifically at 797, 1352, and 1587 cm^{-1} , respectively. The 797 cm^{-1} Raman band is due to Si-C stretching [35] while the bands observed at 1352 and 1587 cm^{-1} are signatures from C sp^2 sites [36]. The peak locations and intensities are diverse owing to bond disorder, bunching of the sp^2 phase, attendance of sp^2 rings or chains, and the sp^2/sp^3 ratio [37]. The origin of the 1360 cm^{-1} peak remains unclear; it could possibly be assigned to the amide mode of the lone sp^2 sites in rings, and not in chains [38]. The peak at 1587 cm^{-1} is due to the bond stretching of all sp^2 atom pairs in both rings and chains, in perfumed and olefinic

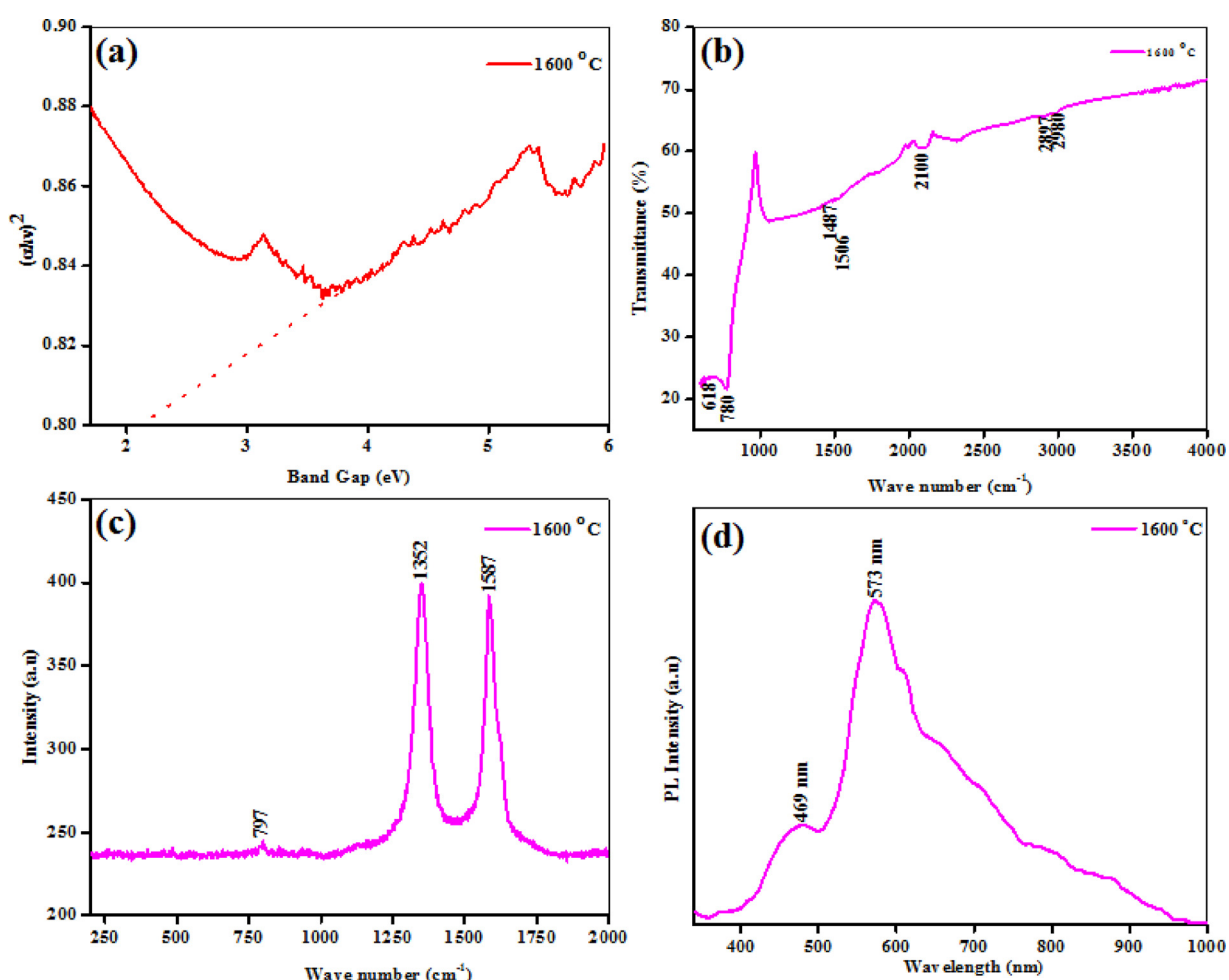


Fig. 4. (a) Bandgap, (b) FT-IR spectrum, (c) Raman spectrum, and (d) PL spectrum SiCN nanowires.

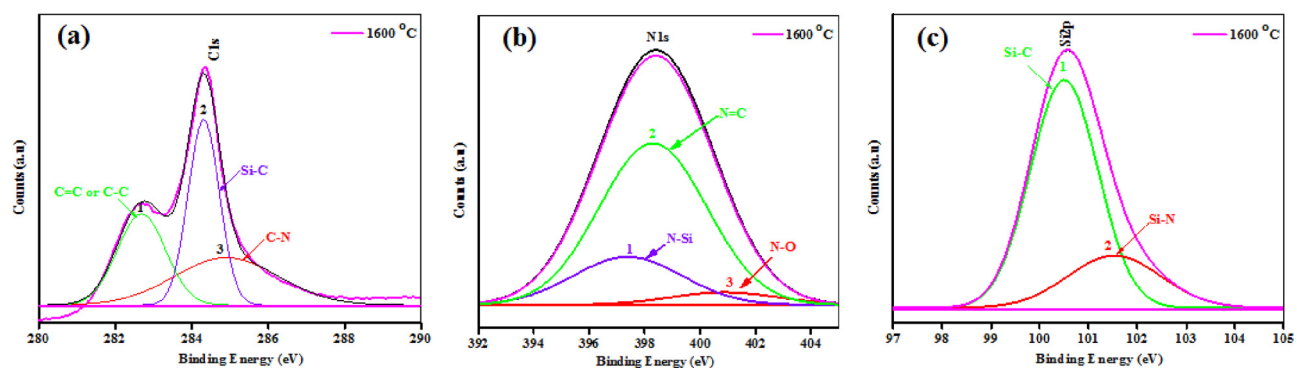


Fig. 5. XPS analysis of SiCN nanowires: (a) C1s core level spectra, (b) N1s core level spectra, and (c) Si2p core-level spectra.

molecules, and it does not require the attendance of six-fold rings [37]. The photoluminescence (PL) spectrum of the sample post-annealed at 1600 °C is presented in Fig. 4(d). It is very interesting to find that the SiCN nanowire shows appreciable PL in the visible region. The PL peaks were observed at 469 and 573 nm, respectively. The emission at 469 nm is attributed to the effects of morphology, orientation, dangling bonds of the facets of the nanowires, and defects [39]; the emission at 573 nm is ascribed to the microcrystalline nature of SiCN [40,41].

3.4. XPS analysis

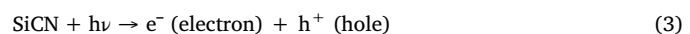
The core level C1s, N1s, and Si2p XPS scans were considered to investigate the chemical bonding states of the samples. Two or three Gaussian peaks in the characteristic spectra in Fig. 5 can sufficiently represent the Si2p, C1s, and N1s spectra. According to investigations by Stoner et al. [42], the C1s binding energies at 282.68, 284.30, and 285.01 eV, as observed in Fig. 5(a), reveal Si-C, C-C or C=C, and C1s-N bonding structures, respectively. The N1s core level peaks at 397.47, 398.35, and 401.12 eV in Fig. 5(b) are attributed to N-Si, N=C, and N-O, respectively. The core peaks at 100.49 and 101.56 eV in the XPS Si2p spectrum shown in Fig. 5(c) are attributed to Si-C and Si-N, respectively. Significantly, there is a separate peak that contests C-Si bonding at 282.68 eV or Si-C bonding at 100.49 eV, and thus includes the existence of Si-C bonds in the SiCN nanowires. The observed binding energy peaks related to the SiCN nanowires are consistent with those reported previously [31,32,43–45]. The area under the peak ranging from 100.49 eV to 101.56 eV is smaller, as shown in Fig. 5(c), indicating that a considerable part of Si within the SiCN sample is bonded to nitrogen. The XPS results clearly suggest that the nitrogen within the SiCN nanowire is bound to both carbon and silicon, and silicon is bound together with silicon and nitrogen in the sample prepared in the present study. Further, the absence of an Si-Si (~99.42 eV) peak suggests that the sample may not contain Si clusters entrenched in the SiCN matrix, and hence the purity of the sample post-annealed at 1600 °C with nanowires formed exclusively of SiCN.

4. Photocatalytic studies

Fig. 6 shows the photocatalytic performance of the SiCN nanowires in the photodegradation of RhB dye under stimulated visible light radiation. Fig. 6(a) shows the optical absorption spectrum of RhB. The RhB dye shows a strong absorption peak at 554 nm; as the visible light irradiation time increased, the intensity of the absorption peak decreased. After 40 min of irradiation, the RhB solution became colorless, signaling the complete degradation of RhB. The change in the degradation (%) of RhB in the presence of the photocatalyst is shown in Fig. 6(b). It is noticed that, with increasing irradiation time, the dye concentration decreases. The degradation performance was first evaluated under the dark condition, where the RhB solution was stirred for 60 min after the addition of the catalyst. During this time, the active

facets of the catalyst were adsorbed by the RhB solution, and as the easily accessible charge carriers take part in the catalytic activity, no noticeable degradation is identified. Under visible light exposure, the SiCN nanowires attained 98.80% degradation of RhB within 40 min. Further, the photocatalytic degradation data were fitted with the Langmuir–Hinshelwood kinetics equation, $\ln(K_t/K_0) = K_b$, where K_t is the pseudo-first order rate constant (min^{-1}), K_0 is the initial concentration of the dye, and C_t is the dye concentration at time t . Fig. 6(c) displays the plot of $\ln(C_t/C_0)$ vs. the irradiation time. The calculated reaction rate constant (K_t) is 0.0841 min^{-1} . To verify the repeatability of the synthesized SiCN nanowires, five repetitive tests were carried out (Fig. 6(d)). After each repetition, the photocatalyst was collected by centrifugation and then re-used in the subsequent tests. After five repetitive tests, the catalytic performance deteriorated only slightly, as shown in Fig. 6(e). From the results, the synthesized SiCN nanowires are found to be active for five cycles with a lower degradation rate compared with the first cycle, but more than 97.85% degradation was achieved within 40 min. The reusability of the catalyst is attributed to the low photo-corrosive effect and high photocatalytic performance of the SiCN nanowires.

The proposed photocatalytic mechanism of SiCN nanowires is as follows. When the photocatalyst material (SiCN) was irradiated with visible light, electrons are excited from the valence band (VB) to the conduction band (CB). As a result, the same number of holes is generated in the VB. During this excitation, some of the electrons moved to the CB, while the other electrons were confined by oxygen vacancies below the surface of the catalyst. The trapped electrons and CB electrons were stimulated together to the surface of the catalyst and confined by the oxygen vacancies on the surface. The O₂ molecules were trapped by the oxygen vacancies existing in air, which leads to the development of superoxide radicals (O₂^{•-}). The oxygen molecules in the RhB dye interacted with the oxygen vacancies present on the surface, which further converted them into superoxide radicals. Likewise, the holes were confined by –OH groups or H₂O molecules to generate hydroxyl radicals (OH^{•+}). Lastly, the produced superoxide and hydroxyl radicals interacted with the pollutant to degrade it efficiently. The complete degradation mechanism for RhB dye can be understood via following reactions with SiCN:



The stability of the SiCN nanowires after the photocatalytic activity was investigated by XRD and XPS (Fig. 7). The structural study reveals

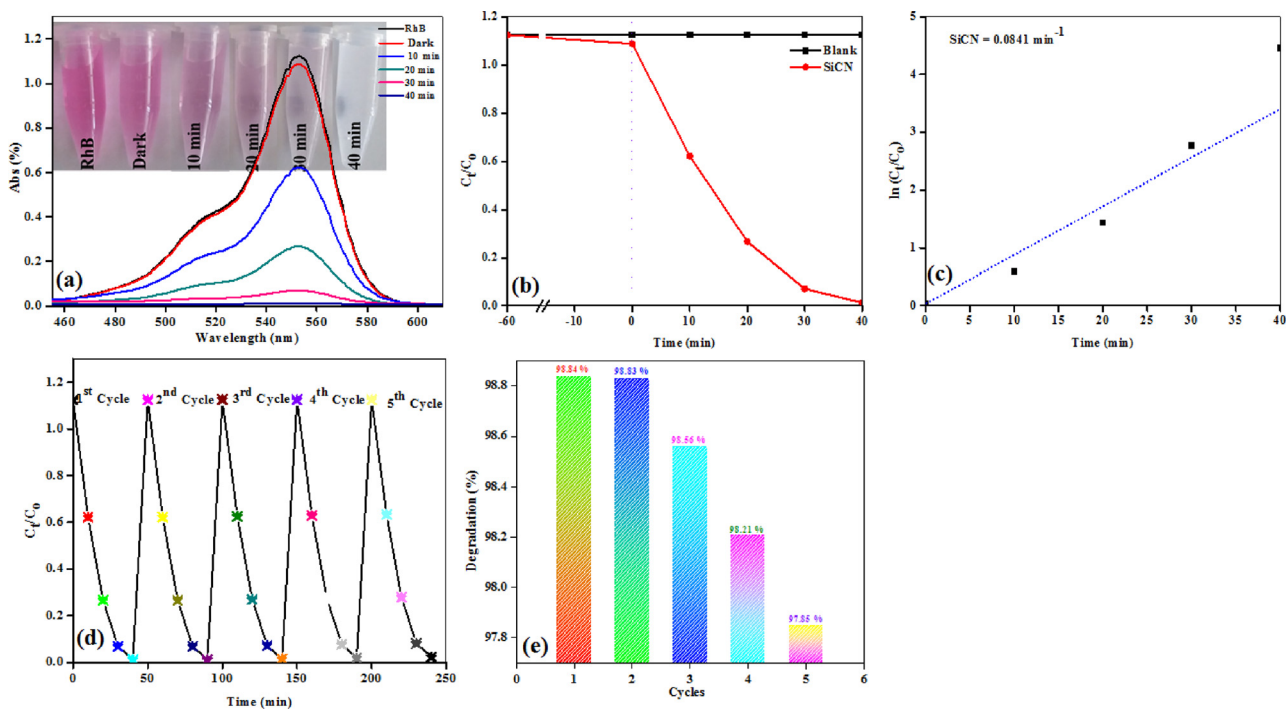


Fig. 6. (a) Absorption spectra corresponding RhB degradation, (b) photocatalytic degradation of RhB, (c) the kinetics plot of RhB degradation, (d) the photocatalyst recycle analysis, and (e) degradation percentages under repetitive cycles.

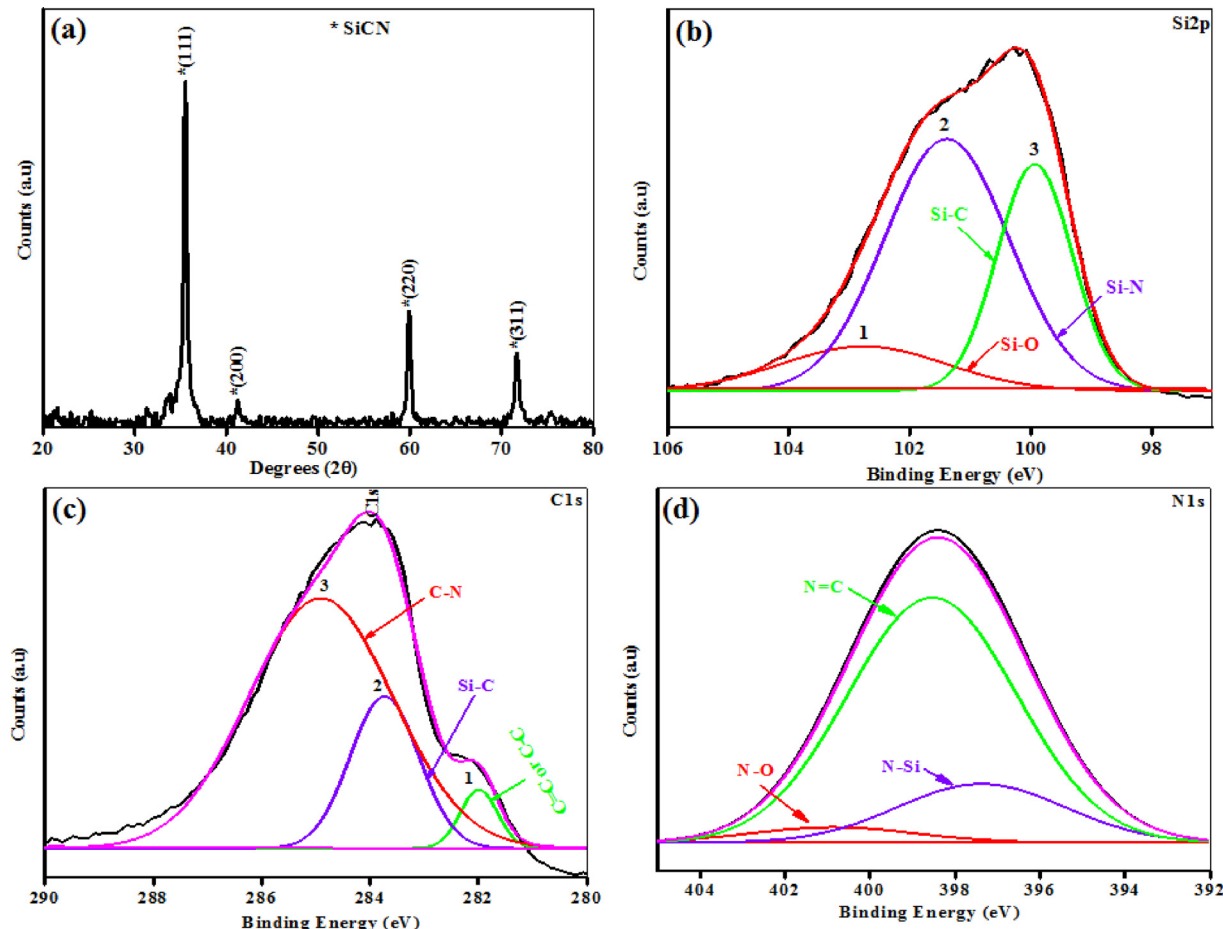


Fig. 7. Analysis of the stability of SiCN nanowires after dye degradation: (a) XRD spectrum, (b) Si2p core level spectra, (c) C1s core level spectra, and (d) N1s core level spectra.

no change in the crystalline structure (Fig. 7(a)). The characteristic peaks of the (111), (200), (220), and (311) planes of the cubic phase of SiCN (JCPDS file No.: 74-2308) were observed at 35.53° , 41.20° , 60.07° , and 71.72° , respectively. These peaks precisely matched with the XRD peaks observed before the activity test. In order to compare the elemental bonding in the SiCN nanowires, XPS analysis was carried out before and after the photocatalytic activity. The core level XPS spectra corresponding to Si2p, C1s, and N1s peaks are shown in Fig. 7(b–c). The Si2p core level peak in the XPS spectrum (Fig. 7(b–c)) can be deconvoluted into three peaks at 102.78, 101.48, and 100.01 eV related to Si-C, Si-N, and Si-O, respectively. Compared with the Si2p core spectrum before degradation, the additional Si2p peak at 102.78 eV in the spectrum obtained after the degradation could be due the oxygen adsorbed during the photocatalytic activity test [31]. The remaining peaks of Si2p at 101.48 and 100.01 eV matched the Si2p peaks of the sample before the activity test. The binding energy peaks of C1s and N1s of SiCN after the activity test are located at 282.01, 283.73, 284.89, 397.36, 398.39, and 400.03 eV, and are attributed to Si-O, C-C, C-N, N-Si, N=C, and N-O, respectively. These C1s and N1s peaks agree well with the C1s and N1s peaks of the sample before their use in dye degradation.

5. Photoelectrocatalytic studies

The morphology of the electrode and the type of electrolyte are vital because the photoelectrochemical water splitting activity is highly influenced by the microstructure of the catalyst and the type of the electrolyte used [46]. Here, electrodes with SiCN nanowire morphology were tested in various electrolytes such as NaOH, KOH, and Na_2SO_4 to estimate the photoelectrocatalytic activity in terms of surface reactions occurring near the SiCN nanowires. Although it needs to provide insight on the initial mechanism which accounts for the efficient water splitting activity. This initial reaction mechanism defines the pathway for the optimization of efficient electrolytes for photoelectrochemical water splitting.

Fig. 8 shows the role and impact of Na_2SO_4 , KOH, and NaOH electrolytes on the water splitting process in the presence of SiCN

nanowires. The water splitting activity varied with the type of electrolyte. The SiCN nanowire in KOH showed significantly improved performance, which is mainly attributed to the high electrolyte conductivity due to the rapid transportation of ions [47]. Firstly, C-V studies were performed for SiCN nanowires in various electrolytes under dark and illuminated states, as shown in Fig. 8(a–c). Clearly, the highest incident photon absorption and photocurrent changes were observed in aqueous KOH electrolyte. The surface stability of the SiCN nanowires in KOH electrolyte results in increased conductivity than in other electrolytes. C-V analysis in terms of time-dependent photocurrents are shown in Fig. S3(a–c). This analysis shows that better photocurrent was obtained by SiCN nanowires in KOH electrolyte than in others. The I-V characteristics of the SiCN nanowires in different electrolytes under dark and illuminated states are shown in Fig. 8(d–f). The I-V results show photocurrent densities similar to those observed in the C-V analysis, indicating that the SiCN nanowires have superior light absorption property in KOH medium. I-V analyses in terms of time-dependent current densities (Fig. S4(a–c)) also show that the catalyst has better light absorption activity in KOH electrolyte than in NaOH or Na_2SO_4 . These results are further supported by the ΔJ values evaluated from the variations in photocurrent under dark and illuminated states. The variations in ΔJ values are similar for both C-V and I-V analyses, as presented in Tables 1 and 2. It is clear from Tables 1 and 2 that SiCN nanowires in the KOH electrolyte show the most stable photoresponse and photocurrent than in other electrolytes. The variations in ΔJ for the SiCN nanowires in aqueous KOH are approximately 0.04 and 0.04 from C-V and I-V analyses, respectively, which are higher than in other electrolytes. Among the tested electrolytes, the SiCN nanowires showed the most stable photo-absorption in the KOH electrolyte.

To further confirm the effect of the electrolyte on photoresponse, we measured the photocurrent densities of the SiCN nanowires in various electrolytes (Na_2SO_4 , KOH, and NaOH) under light-on and light-off states as a function of time. Fig. 9(a) shows the variations in the photocurrent densities and stability of the SiCN nanowires. The photocurrents are not effective in the Na_2SO_4 electrolyte, whereas effective photocurrents are achieved in NaOH and KOH electrolytes. Between NaOH and KOH, the higher photocurrent was generated in KOH

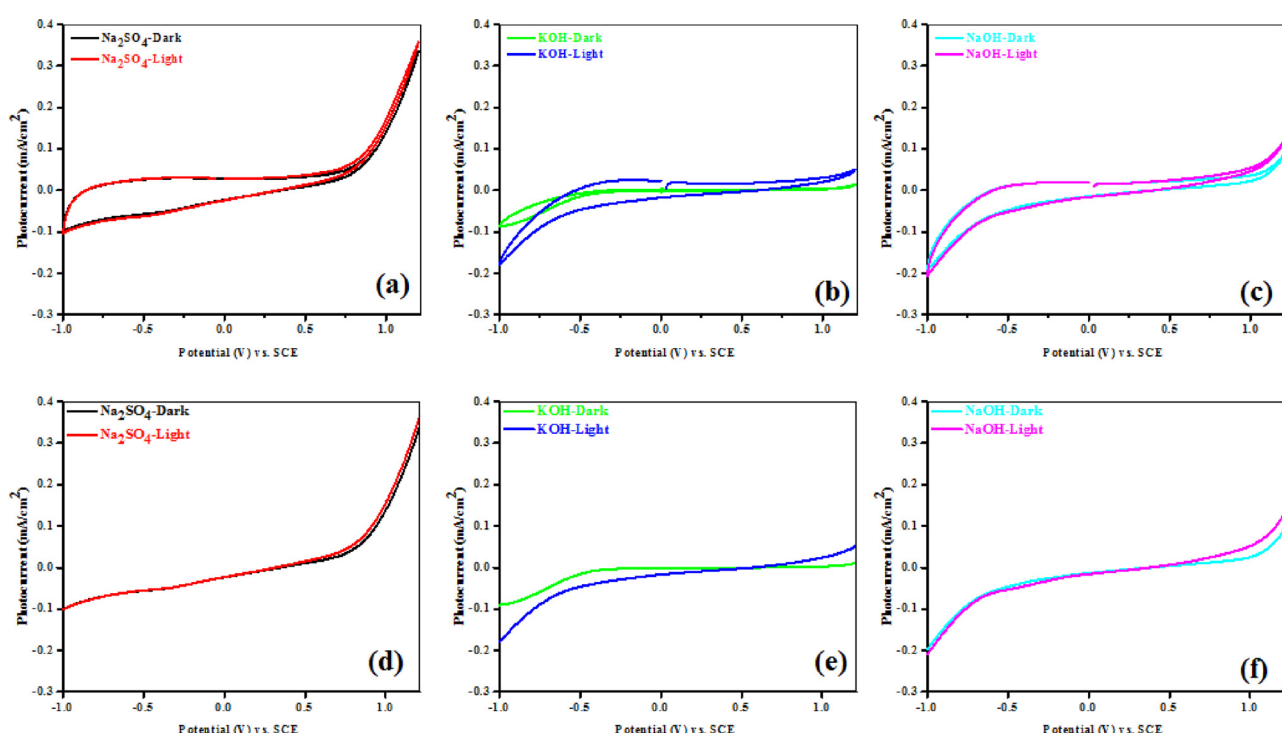


Fig. 8. PEC studies on SiCN nanowires in various electrolytes under dark and illuminated states: (a–c) C-V analysis, (d–f) I-V analysis.

Table 1

Photocurrents obtained by C-V analysis for SiCN nanowires in various electrolytes under dark and illuminated states.

Electrolyte	Dark (mA cm^{-2})	Light (mA cm^{-2})	ΔJ (mA cm^{-2})
Na_2SO_4	0.34	0.36	0.02
KOH	0.01	0.05	0.04
NaOH	0.08	0.12	0.03

Table 2

Photocurrents obtained by I-V analysis for SiCN nanowires in various electrolytes under dark and illuminated states.

Electrolyte	Dark (mA cm^{-2})	Light (mA cm^{-2})	ΔJ (mA cm^{-2})
Na_2SO_4	0.33	0.35	0.02
KOH	0.01	0.05	0.04
NaOH	0.09	0.12	0.03

medium, implying an additional concentration of hydroxide ions in the KOH electrolyte. As KOH is more conductive, the charge can be transported efficiently through the electrolyte, and thus significant photocurrent is produced on the SiCN nanowire surfaces. These results correlate well with the C-V, I-V, and ΔJ analyses.

In order to estimate the hydrogen evolution reaction mechanism of the SiCN nanowires, Tafel plots were recorded using the aforementioned electrolytes and Tafel slopes were obtained. The linear fitting was made using the Tafel equation $h = a + b \log j$ to obtain the Tafel slopes, exchange current density (j_0), and limiting diffusion current density (J_{lim}) (Fig. S5(a)). In general, a lower Tafel slope value indicates that the catalyst requires low applied potential to produce a characteristic current. The j_0 represents the catalyst electron transfer rate of the catalyst, and J_{lim} is associated with the diffusion coefficient, which is similar to that of the electrolyte [48,49]. However, the Tafel plots should be interpreted carefully because the Tafel slope varies in a complex manner depending on several parameters such as the reaction pathway, catalyst preparation, adsorption conditions of the active site, and catalyst categories [50]. The Tafel plots of SiCN nanowires in various electrolytes are shown in Fig. 9(b). The shift toward the anodic side is observed upon changing the electrolyte, i.e., in the order of $\text{Na}_2\text{SO}_4 \rightarrow \text{KOH} \rightarrow \text{NaOH}$, indicating a change in the rate-determining step of the reaction [51]. The Tafel slopes of SiCN nanowires under dark and illuminated conditions in various electrolytes estimated from Fig. 9(b) and Fig. S5(b) are listed in Table 3. The results reveal that

Table 3

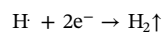
Photocurrents obtained by Tafel analysis for SiCN nanowires in various electrolytes under dark and illuminated states.

Electrolyte	Tafel slopes		j_0		J_{lim}	
	Dark mVdec ⁻¹	Light mVdec ⁻¹	Dark mA cm^{-2}	Light mA cm^{-2}	Dark mA cm^{-2}	Light mA cm^{-2}
Na_2SO_4	96.0	88.24	−3.81	−3.73	−1.98	−1.93
KOH	78.32	68.13	−3.62	−3.17	−1.62	−1.54
NaOH	82.51	75.12	−3.57	−3.33	−1.63	−1.56

SiCN nanowires in 0.1 M KOH electrolyte show the lowest Tafel slopes (dark: 78.32 mVdec⁻¹; light: 68.13 mVdec⁻¹) in both states, which implies that it requires low applied potential to produce current. The above analysis indicates that KOH is the best electrolyte for the SiCN catalyst. The j_0 and J_{lim} have estimated also in both states, and the results are listed in Table 3. The highest j_0 and J_{lim} values were obtained for SiCN nanowires in 0.1 M KOH, indicating that the SiCN nanowire catalyst exhibits better exchange current density and limiting diffusion current density in this electrolyte than in other electrolytes.

A schematic of the three-electrode cell, which includes the photoelectrochemical setup and the catalytic mechanism, is shown in Fig. 10. A typical cell filled with 0.1 M KOH (80 mL) electrolyte consists of Ag/AgCl as the reference electrode, Pt as the counter electrode, and the SiCN nanowire coated on ITO-glass and masked by exposing 1 cm² active area as the working electrode. The entire three-electrode cell was connected to a potentiostat. A light source with wavelengths greater than 450 nm was used in this PEC study, as represented in the schematic of Fig. 10. When 1 cm² of the active area of the SiCN nanowire catalyst was illuminated by visible light, the electrons were excited from the VB to CB; at the same time, an equal number of holes was generated in the VB. During the activity, the generated holes and electrons were actively involved in the reduction and oxidation processes at the CB and VB of the SiCN nanowire catalyst. The following reactions occurred at the surface of the counter and working electrodes:

At the surface of the counter electrode:



At the surface of the working electrode:

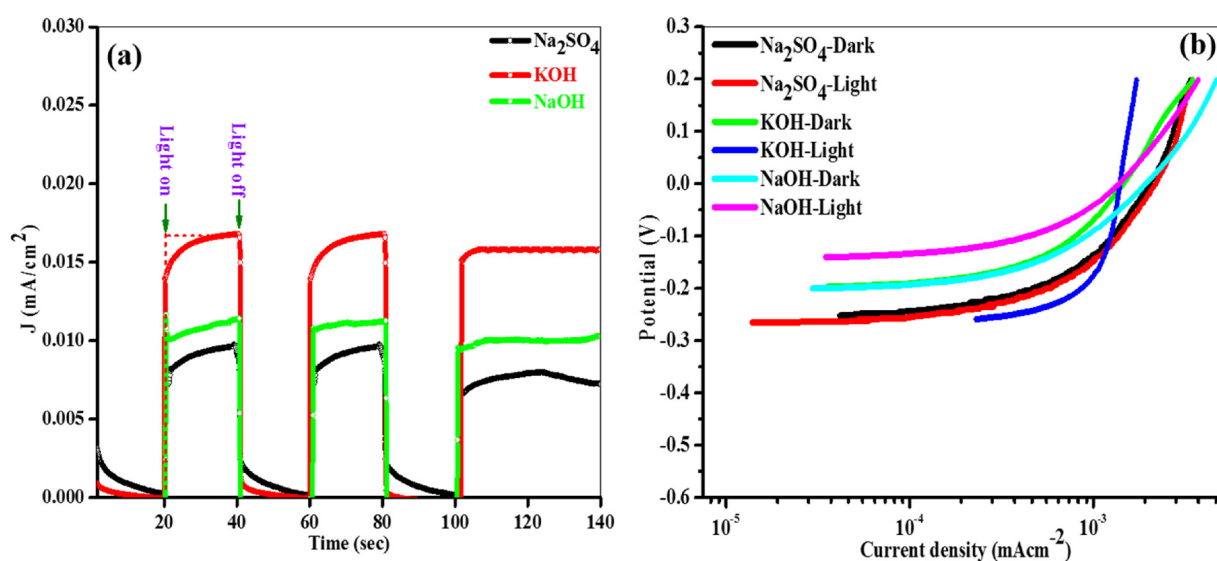
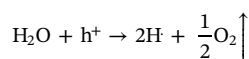


Fig. 9. PEC studies on SiCN nanowires in various electrolytes under dark and illuminated states: (a) I-t plots, and (b) linear Tafel Plots.

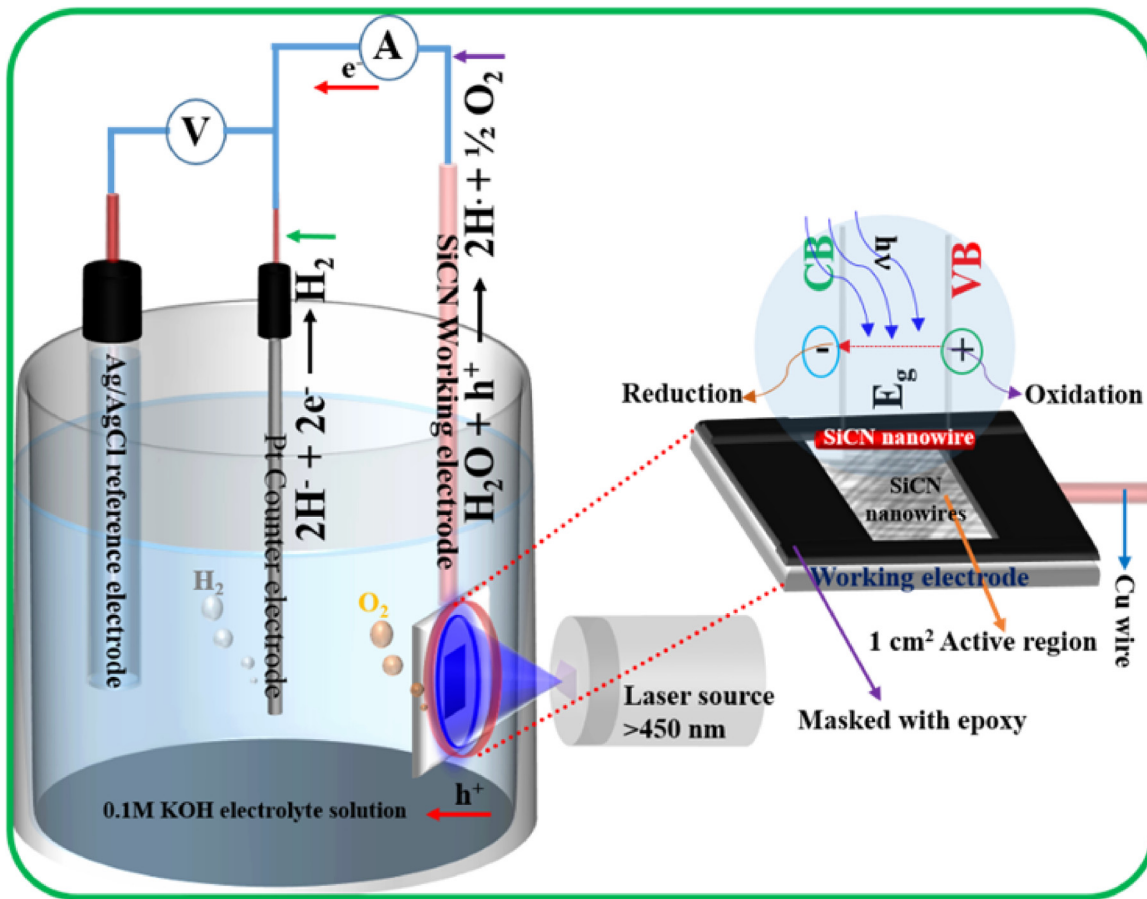


Fig. 10. Schematic representation of the PEC mechanism of SiCN nanowires with a PEC measurement setup.

6. Supercapacitance analysis

The electrochemical properties of the SiCN nanowires electrode were investigated using the CV and GVD techniques to examine the performance of nanowires as a supercapacitor. Fig. 11(a–b) shows the CV curves of the SiCN electrode, recorded at scan rates of 10, 20, 40, 60, 80, 100, 200, 400, 600, 800 and 1000 mVs⁻¹ within a applied potential window of -0.10 to +0.50 V, in 0.1 M aqueous KOH solution at room temperature. The CV curves of SiCN increased with scan rate, and is close to an ideal rectangle shape, signifying excellent supercapacitive characteristics. Even at a very high scan rate of 1000 mVs⁻¹, the CV curve of SiCN still shows a good rectangle shape, demonstrating outstanding rate performance (Fig. 11(b)). This is also evidence that the current response of the working electrode increases with increasing scan rates, and the shapes of the CV curves remain constant throughout the wide scan rates from 10 to 1000 mVs⁻¹. The first and 1000th cycles performed at a constant scan rate of 200 mVs⁻¹ show an invariant good rectangle shape throughout the cycles (Fig. 11(c)). The complete 1000 cycles performed at a constant scan rate of 200 mVs⁻¹ are in shown in Fig. S6, which indicate a rectangle shape. Lower scan rates have lower current mainly because of the dense diffusion layer developed on the surface of the working electrode, which limits the electrolyte flux toward the electrode. However, at higher scan rates, enhanced current occurs because the diffusion layer cannot develop largely on the surface of the electrode, assisting higher electrolyte flux [52]. The significant increase in current has been observed in CV curves in the case of the SiCN nanowire electrode with the scan rates. Furthermore, unique nanostructures like the wires, rods, and tubes of electrode materials can store electrolytic ions successfully, and also enables ion transfer to the inner sides of the electrode by restricting the ion diffusion pathway even at larger scan rates [52,53]. The specific capacitance of SiCN

reached ~32 mFcm⁻² at 10 mVs⁻¹, but decreased with increasing scan rate to reach 9.41 mFcm⁻² for 1000 mVs⁻¹. The dependence of SiCN specific capacitance vs. scan rate is plotted in Fig. 11(d), suggesting that the specific capacitance of the SiCN significantly depends on the scan rate. Figure S7 shows the specific capacitance vs. the number of cycles recorded at 200 mVs⁻¹, observed a constant specific capacitance of 11.25 mFcm⁻² up to 1000 cycles.

Fig. 11(e) shows the GCD cycle of the SiCN nanowires electrode at various current densities ranging from 2 to 12 mAcm⁻² in the applied voltage window ranging from +0.50 to -0.10 V. It was observed that the decreasing discharge time of SiCN corresponds to current densities; the maximum discharge time was observed at 2 mAcm⁻² within the applied voltage window. The insert of Fig. 11(e) shows the GCD cycle of the SiCN nanowires electrode at constant current density of 5 mAcm⁻², observed at frequently discharge time up to 1000 cycles. The specific capacitance vs. current densities is shown in Fig. 11(f). Here, the specific capacitance obtained from the GCD have similar trends, as shown in Fig. 11(d). However, the specific capacitance obtained from GCD (35.61 mFcm⁻² at 10 mVs⁻¹) is five times of the capacitance obtained from the CV curves (188.81 mFcm⁻² at 2 mAcm⁻²). The constant specific capacitance of SiCN nanowires was 52.2 ± 1.2 mFcm⁻² at 5 mAcm⁻² up to 1000 cycles (shown in the inset of Fig. 11(f)), indicating the stability of electrode materials.

7. Conclusions

SiCN samples with ultra-long nanowire structure and varying diameters were prepared by high-energy ball milling and post-annealing. The formation and morphology of the nanowires were confirmed by XRD, FESEM, and TEM studies. The SiCN nanowires showed the highest RhB dye degradation of ~99% in 40 min in the presence of visible light.

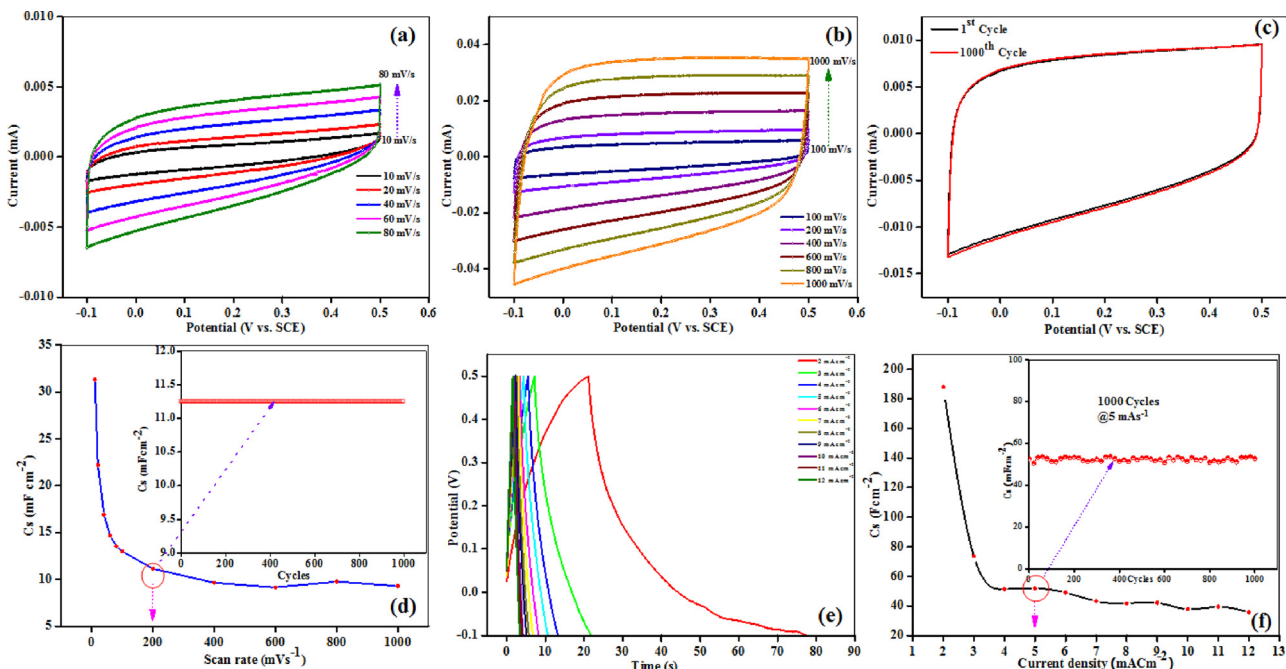


Fig. 11. (a, b) Cyclic voltammetry curves of the SiCN nanowires electrode at various scan rates in a 0.1 M KOH solution at room temperature; (c) cyclic voltammetry curves 1st and 1000 cycles at a constant scan rate of 200 mVs^{-1} for comparison; (d) variation of specific capacitance with scan rates, (inset of panel a) variation of specific capacitance vs. cycles at a constant scan rate of 200 mVs^{-1} ; (e) charge/discharge curves of the SiCN nanowires electrode at various current densities; and (f) variation of specific capacitance with current densities, (inset of panel a) variation of specific capacitance vs. cycles at a constant current density of 5 mA cm^{-2} .

The investigation of the photoelectrochemical properties of SiCN nanowires in various electrolytes revealed that the Tafel plots, cyclic voltammograms ($C-V$), linear sweep voltammograms ($I-V$), and time-resolved photocurrents ($I-t$) were strongly dependent on the type of electrolyte. The system of SiCN nanowires in KOH electrolyte has the highest photocurrent density. The SiCN nanowires exhibited outstanding photoelectrochemical stability up to 140 s of reaction as well as high incident charge conversion efficiency. The SiCN nanowires can promote the separation of charge pairs, encouraging applications in photocatalytic and photoelectrochemical water splitting. In addition, the maximum specific capacitance of SiCN nanowires is 188.81 mF cm^{-2} at 2 mA cm^{-2} , which is five times the specific capacitance achieved from CV curves. In CV and GCD for 1000 cycles at 200 mVs^{-1} and 5 mA cm^{-2} , the specific capacitance was almost constant at 11.25 and 52.23 mF cm^{-2} , respectively.

Acknowledgments

This work was supported by the National Research Foundation of Korea grant funded by the Korea government (No. 2015R1A2A2A01003741, 2015R1C1A2A01052256, 2018R1D1A1B07048307 and 2017R1A4A1015581).

Appendix A. Supplementary data

Supplementary material related to this article can be found, in the online version, at doi:<https://doi.org/10.1016/j.apcatb.2018.06.061>.

References

- [1] M. Gratzel, Photoelectrochemical cells, *Nature* 414 (2001) 338–344.
- [2] A. Fujishima, K. Honda, Electrochemical photolysis of water at a semiconductor electrode, *Nature* 238 (1972) 37–38.
- [3] X. Chen, C. Li, M. Gratzel, R. Kostecki, S.S. Mao, Nanomaterials for renewable energy production and storage, *Chem. Soc. Rev.* 41 (2012) 7909–7937.
- [4] S.U.M. Khan, M. Al-Shahry, W.B. Ingler Jr, Efficient photochemical water splitting by a chemically modified n-TiO₂, *Science* 297 (2002) 2243–2245.
- [5] X. Chen, L. Liu, P.Y. Yu, S.S. Mao, Increasing solar absorption for photocatalysis with black hydrogenated titanium dioxide nanocrystals, *Science* 331 (2011) 746–750.
- [6] Y. Zhang, T. Xia, P. Wallenmeyer, C.X. Harris, A.A. Peterson, G.A. Corsiglia, J. Murowchick, X. Chen, Photocatalytic hydrogen generation from pure water using silicon carbide nanoparticles, *Energy Technol.* 2 (2014) 183–187.
- [7] Z. Kang, C.H.A. Tsang, N.-B. Wong, Z. Zhang, S.-T. Lee, Silicon quantum dots: a general photocatalyst for reduction, decomposition, and selective oxidation reactions, *J. Am. Chem. Soc.* 129 (2007) 12090–12091.
- [8] C. He, X. Wu, J. Shen, P.K. Chu, High-efficiency electrochemical hydrogen evolution based on surface autocatalytic effect of ultrathin 3C-SiC nanocrystals, *Nano. Lett.* 12 (2012) 1545–1548.
- [9] H. Yamashita, H. Nose, Y. Kuwahara, Y. Nishida, S. Yuan, K. Mori, TiO₂ photocatalyst loaded on hydrophobic Si₃N₄ support for efficient degradation of organics diluted in water, *Appl. Catal. A: Gen.* 350 (2008) 164–168.
- [10] A.N. Murashkevich, O.A. Alisienok, I.M. Zharskii, Physicochemical and photocatalytic properties of nanosized titanium dioxide deposited on silicon dioxide microspheres, *Kinet. Catal.* 52 (2011) 809–816.
- [11] Y. Nariki, Y. Inoue, K. Tanaka, Production of ultra-fine SiC powder from SiC bulk by arc-plasma irradiation under different atmospheres and its application to photocatalysts, *J. Mater. Sci.* 25 (1990) 3101–3104.
- [12] C.W. Chen, C.C. Huang, Y.Y. Lin, L.C. Chen, K.H. Chen, W.F. Su, Optical properties and photoconductivity of amorphous silicon carbon nitride thin film and its application for UV detection, *Diam. Relat. Mater.* 14 (2005) 1010–1013.
- [13] L.J. Chai, L.X. Feng, Z.Z. Hong, G.H. Xi, Y.M. Sheng, The preparation and characterization of amorphous SiCN thin films, *Wuhan University J. Nat. Sci.* 6 (2001) 665–669.
- [14] Y. Peng, J. Zhou, J. Gong, Q. Yu, Microstructure and optical properties of SiCN thin films deposited by reactive magnetron sputtering, *Mater. Lett.* 131 (2014) 148–150.
- [15] E. Tomasella, F. Rebib, M. Dubois, J. Cellier, M. Jacquet, Structural and optical properties studies of sputtered a-SiCN thin films, *J. Phys.: Conf. Ser.* 100 (2008) 082045.
- [16] Y. Peng, J. Zhou, B. Zhao, X. Tan, Z. Zhang, Structural and optical properties of the SiCN thin films prepared by reactive magnetron sputtering, *Appl. Surf. Sci.* 257 (2011) 4010–4013.
- [17] L. David, K.M. Shareef, M.A. Abass, G. Singh, Three-dimensional polymer-derived ceramic/graphene paper as li-ion battery and supercapacitor electrode, *RSC Adv.* 6 (2016) 53894–53902.
- [18] R. Kolb, C. Fasel, V.L. Kunzmann, R. Riedel, SiCN/C-ceramic composite as anode material for lithium ion batteries, *J. Eur. Ceram. Soc.* 26 (2006) 3903–3908.
- [19] D. Su, Y.-L. Li, Y. Feng, J. Jin, Electrochemical properties of polymer-derived SiCN materials as the anode in lithium ion batteries, *J. Am. Ceram. Soc.* 92 (2009) 2962–2968.
- [20] Z. Su, C. Yang, B. Xie, Z. Lin, Z. Zhang, J. Liu, B. Li, F. Kang, C.P. Wong, Scalable fabrication of mno₂ nanostructure deposited on free-standing Ni nanocone arrays for ultrathin, flexible, high-performance micro-supercapacitor, *Energy Environ. Sci.* 7 (2014) 2652–2659.
- [21] N. Singh, K. Singh, D. Kaur, Bipolar resistive switching characteristics of silicon

- carbide nitride (SiCN)-based devices for nonvolatile memory applications, *Ceram. Int.* 43 (2017) 8970–8974.
- [22] M. Sreedhar, J. Brijitta, I.N. Reddy, M. Cho, J. Shim, P. Bera, B.N. Joshi, S.S. Yoon, Dye degradation studies of Mo-doped TiO₂ thin films developed by reactive sputtering, *Surf. Interface Anal.* 50 (2018) 171–179.
- [23] Q. Zhang, D. Jia, Z. Yang, D. Cai, R.M. Laine, Q. Li, Y. Zhou, Facile synthesis, microstructure and photophysical properties of core-shell nanostructured (SiCN)/BN nanocomposites, *Sci. Rep.* 7 (2017) 39866.
- [24] P. Wang, L. Cheng, L. Zhang, Lightweight, flexible SiCN ceramic nanowires applied as effective microwave absorbers in high frequency, *Chem. Eng. J.* 338 (2018) 248–260.
- [25] K. Cai, L. Huang, A. Zhang, J. Yin, H. Liu, Synthesis, characterization, and electrical properties of SiCN nanowires, *Cryst. Growth Des.* 8 (2008) 2144–2149.
- [26] K.F. Cai, L.Y. Huang, A.X. Zhang, J.L. Yin, H. Liu, Ultra long SiCN nanowires and SiCN/SiO₂ nanocables: synthesis, characterization, and electrical property, *J. Nanosci. Nanotechno.* 8 (2008) 6338–6343.
- [27] W. Cheng, X. Ma, Low temperature synthesis of SiCN nanostructures, *Sci. China Ser. E: Technol. Sci.* 52 (2009) 28–31.
- [28] Z. Chen, J. Zhou, X. Song, X. Xu, Y. Liu, J. Song, Z. Ma, E. Xie, The effect of annealing temperatures on morphologies and photoluminescence properties of terbium-doped SiCN films, *Opt. Mater.* 32 (2010) 1077–1084.
- [29] V.L. Nguyen, E. Zera, A. Perolo, R. Campostrini, W. Li, G.D. Soraru, Synthesis and characterization of polymer-derived SiCN aerogel, *J. Eur. Ceram. Soc.* 35 (2015) 3295–3302.
- [30] J.-J. Wu, C.-T. Wu, Y.-C. Liao, T.-R. Lu, L.C. Chen, K.H. Chen, L.-G. Hwa, C.-T. Kuo, K.-J. Ling, Deposition of silicon carbon nitride films by ion beam sputtering, *Thin Solid Films* (355–356) (1999) 417–422.
- [31] N. Feng, Y. Feng, Y. Wei, X. Zhou, Preparation and electrochemical performance of a porous polymer-derived silicon carbonitride anode by hydrofluoric acid etching for lithium ion batteries, *RSC Adv.* 4 (2014) 23694.
- [32] Y. Feng, N. Feng, Y. Wei, Y. Bai, Preparation and improved electrochemical performance of SiCN-graphene composite derived from poly(silylcarbodiimide) as Li-ion battery anode, *J. Mater. Chem. A* 2 (2014) 4168.
- [33] Q. Zhang, Z. Yang, D. Jia, Q. Chen, Y. Zhou, Synthesis and structural evolution of dual-boron-source-modified polysilazane derived SiBCN ceramics, *New J. Chem.* 40 (7034) (2016).
- [34] B.P. Swain, N.M. Hwang, Study of structural and electronic environments of hydrogenated amorphous silicon carbonitride (a-SiCN: H) films deposited by hot wire chemical vapor deposition, *Appl. Surf. Sci.* 254 (2008) 5319–5322.
- [35] J. Bandet, B. Despax, M. Caumont, Nitrogen bonding environments and local order in hydrogenated amorphous silicon nitride films studied by Raman spectroscopy, *J. Appl. Phys.* 85 (1999) 7899.
- [36] S.H. Hong, J. Winter, Micro-Raman spectroscopy on a-C:H nanoparticles, *J. Appl. Phys.* 98 (2005) 124304.
- [37] A.C. Ferrari, J. Robertson, Interpretation of Raman spectra of disordered and amorphous carbon, *Phys. Rev. B* 61 (2000) 14095.
- [38] J. Robertson, Diamond-like amorphous carbon, *Mater. Sci. Eng. R.* 37 (2002) 129–281.
- [39] J. Chen, R. Wu, G. Yang, Y. Pan, J. Lin, L. Wu, R. Zhai, Synthesis and photoluminescence of needle-shaped 3C-SiC nanowires on the substrate of PAN carbon fiber, *J. Alloy. Compd.* 456 (2008) 320–323.
- [40] K. Zekentes, K. Rogdakis, SiC nanowires: material and devices, *J. Phys. D: Appl. Phys.* 44 (2011) 133001.
- [41] J. Chen, W. Tang, L. Xin, Q. Shi, Bandgap characterization and photoluminescence properties of SiC nanowires, *Appl. Phys. A* 102 (2011) 213–217.
- [42] B.R. Stoner, G.H. Ma, S.D. Wolter, J.T. Glass, Characterization of bias-enhanced nucleation of diamond on silicon by *in vacuo* surface analysis and transmission electron microscopy, *Phys. Rev. B* 45 (1992) 11067.
- [43] S.K. Mishra, A.S. Bhattacharyya, P.K.P. Rupa, L.C. Pathak, XPS studies on nanocomposite Si-C-N coatings deposited by magnetron sputtering, *Nanosci. and Nanotechno. Lett.* 4 (2012) 352–357.
- [44] J.-J. Wu, C.-T. Wu, Y.-C. Liao, T.-R. Lu, L.C. Chen, K.H. Chen, L.-G. Hwa, C.-T. Kuo, K.-J. Ling, Deposition of silicon carbon nitride films by ion beam sputtering, *Thin Solid Films* (355–356) (1999) 417–422.
- [45] X.-M. He, T.N. Taylor, R.S. Lillard, K.C. Walter, M. Nastasi, Bonding structure and properties of ion enhanced reactive magnetron sputtered silicon carbonitride films, *J. Phys.: Condens. Matter.* 12 (2000) L591–L597.
- [46] C. Ding, J. Shi, Z. Wang, C. Li, Photoelectrocatalytic water splitting: significance of cocatalysts, electrolyte, and interfaces, *ACS Catal.* 7 (2017) 675–688.
- [47] R.J. Gilliam, J.W. Graydon, D.W. Kirkb, S.J. Thorpe, A review of specific conductivities of potassium hydroxide solutions for various concentrations and temperatures, *Int. J. Hydrogen Energ.* 32 (2007) 359–364.
- [48] P. Atkins, J.D. Paula, Atkins' Physical Chemistry, 7th ed., Oxford University, UK, 2002.
- [49] M. Zheng, J. Huo, Y. Tu, J. Jia, J. Wu, Z. Lan, An in situ polymerized PEDOT/Fe₃O₄ composite as a Pt-free counter electrode for highly efficient dye sensitized solar cells, *RSC Adv.* 6 (2016) 1637.
- [50] L. Liao, J. Zhu, X. Bian, L. Zhu, M.D. Scanlon, H.H. Girault, B. Liu, MoS₂ formed on mesoporous graphene as a highly active catalyst for hydrogen evolution, *Adv. Funct. Mater.* 23 (2013) 5326–5333.
- [51] L. Guclu, A. Erdohelyi, Springer science & business media, *Catalysis for Alternative Energy Generation*, (2012), pp. 1–538.
- [52] A. Sarkar, A.K. Singh, D. Sarkar, G.G. Khan, K. Mandal, Three-dimensional nanoarchitecture of BiFeO₃ anchored TiO₂ nanotube arrays for electrochemical energy storage and solar energy conversion, *ACS Sustainable Chem. Eng.* 3 (2015) 2254–2263.
- [53] M. Rajkumar, C.-T. Hsu, T.-H. Wu, M.-G. Chen, C.-C. Hu, Advanced materials for aqueous supercapacitors in the asymmetric design, *Prog. Nat. Sci.-Mater. Int.* 25 (2015) 527–544.